CIRP Annals - Manufacturing Technology 74 (2025) 257–261

Contents lists available at ScienceDirect

CIRP Annals - Manufacturing Technology

journal homepage: https://www.editorialmanager.com/CIRP/default.aspx

Enhanced Magnet-aided Laser Induced Plasma Micromachining (E-MLIP) for Expanded Geometric Capabilities

Rajiv Malhotra[a,*], AnandKumar Patel[a], Kiarash Naghavi Khanghah[b], Hongyi Xu[b]

[a] Department of Mechanical and Aerospace Engineering, Rutgers University, USA
[b] School of Mechanical, Aerospace and Manufacturing Engineering, University of Connecticut, USA

Submitted by Alkan Donmez (1), Gaithersburg, USA

ARTICLE INFO

Article history:
Available online 29 April 2025

Keywords:
Laser micro machining
plasma
monitoring

ABSTRACT

Laser Induced Plasma Micro Machining (LIPMM) focusses a laser inside a liquid to create plasma that is used for micromachining with superior multi-material capability. This work subjects the plasma to a novel magnetic field to realize atypically simultaneous enhancement of feature resolution, feature depth and Material Removal Rate beyond the limitations of LIPMM and Direct Laser Ablation. A new physics-based model is established to uncover the mechanism behind this enhancement. Further, an acoustics-based approach is created for quantitative in-situ prediction of feature dimensions while considering unknown phenomenological disturbances in the material removal zone, a capability that lies beyond the state-of-the-art.

1. Introduction

Laser micromachining via Direct Laser Ablation (DLA) is used for manufacturing electronics, metamaterials, solar cells, implants, smart materials, and microfluidics. In these applications the device functionality and cost-effectiveness can be significantly enhanced by simultaneously increasing feature depth, planar resolution ($\propto$ 1/feature width), Material Removal Rate (MRR) and material window beyond the optical and thermal limits imposed by DLA.

Laser Induced Plasma Micro Machining (LIPMM, Fig. 1a) focuses a pulsed laser inside a dielectric liquid to create plasma and uses this plasma to micromachine a workpiece submerged in the liquid [1,2]. Coupling the laser energy into the plasma rather than directly into the workpiece accommodates reflective, transparent, rough, and high ablation threshold materials that cannot be machined by DLA with the same laser and optics hardware [1,3]. This enables cost-effective expansion of the material window by enabling use of the same laser and optics for diverse materials.

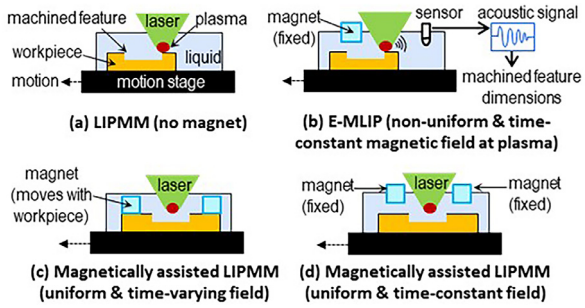

Fig. 1. Working principle of E-MLIP compared to LIPMM & M-LIPMM.

But, for the same process parameters and hardware, LIPMM and DLA yield the same feature dimensions and MRR due to physical constraints [4], e.g., the optics limits the plasma size and thus the feature dimensions. Magnetically assisted LIPMM (M-LIPMM) imposes a magnetic field on the plasma and experimentally characterizes the effects of the magnetic field's magnitude on feature dimensions [5–9]. But the field configurations used till date cannot increase feature resolution, depth, and MRR concurrently. DLA based on dual pulses [10], near fields [11], magnetic fields [12], and liquid immersion [13] has the same limitation. Bessel beam DLA resolves this issue but only for transparent workpieces, thus sacrificing the multimaterial capability of LIPMM [14].

This paper creates an Enhanced Magnet-aided Laser Induced Plasma micromachining (E-MLIP) process that augments the multimaterial capabilities of LIPMM by simultaneously enhancing the feature depth, resolution and MRR beyond the limits of DLA and LIPMM. The novelty lies in imposing a spatially non-uniform magnetic field with constant magnitude on the plasma. This is achieved by fixing one magnet relative to the plasma and moving the workpiece to remove material (Fig. 1b). In contrast, the state-of-the-art imposes a spatially uniform magnetic field that is either time-varying (magnets on workpiece, Fig. 1c) or time-constant (magnets on laser, Fig. 1d). Experiments are performed to characterize the capabilities of E-MLIP. A novel physics-based model is created to reveal why E-MLIP enhances geometric capabilities. An acoustic sensing approach is developed

* Corresponding author.
E-mail address: rajiv.malhotra@rutgers.edu (R. Malhotra).

https://doi.org/10.1016/j.cirp.2025.04.065

for in-situ quantitative prediction of feature dimensions in light of disturbances during material removal, a capability that is beyond the state-of-the-art.

2. Methods

2.1. Experimental methods

Fig. 1b illustrates the experimental setup for E-MLIP. The magnet was fixed at 3 mm from the laser's stationary focal spot. The workpiece (Aluminum 6061) was submerged in the dielectric liquid inside a container. The container was placed on a motion stage. Thus, stage speed and laser speed are interchangeable here. An Acoustic Emission (AE) sensor was mounted at a fixed distance from the focal spot with its sensing element fully inside the liquid. Machining and signal collection were coordinated by a Transistor-to-Transistor Logic (TTL) signal. The signal acquisition rate was orders of magnitude greater than the laser frequency. Table 1 lists additional experimental details.

Table 1
Details of experimental setup and process parameters

Laser	3 ns pulse duration, 526 nm wavelength, 100 µm spot diameter. Laser speed S: 0.10–0.65 mm/s, laser pulse energy E: 20–50 mJ, laser pulse frequency ν: 5, 10, 20 Hz.
Liquid	Deionized water, 2 mm thickness above workpiece
Magnet	Permanent, rectangular, surface flux density of 0.7 Tesla.
AE sensor	Aquarian model AS-1, 1 Hz-100 kHz range, 40 μV/Pa.

Initial experiments machined holes for the magnet-plasma configurations shown in Fig. 2. The measured hole dimensions were used to identify the optimal configuration for E-MLIP of microchannels. The channels were machined using one laser pass and combinations of laser speed, energy, and frequency listed in Table 1. The machined channel's width and depth were measured using a white light interferometer and averaged across ten cross-sections along its length. The volumetric MRR was calculated as the product of channel width, channel depth, and laser speed. LIPMM was performed with the same process parameters. This enabled comparison of E-MLIP to LIPMM and DLA as these two processes yield the same feature dimensions for same process parameters and hardware [4,15].

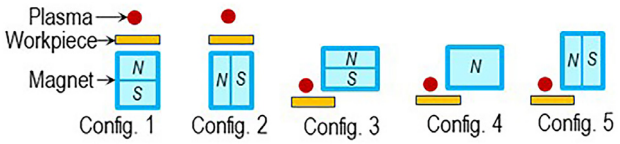

Fig. 2. Magnet-plasma configurations examined for E-MLIP.

2.2. Physics-based modelling

The plasma shape in E-MLIP limits the minimum width and maximum depth of the machined features. The plasma shape is governed by the following physics [16]. Magnetic pressure deforms the plasma since electromagnetically the plasma behaves like a mass of electrons in a magnetic field. This alters the plasma's density, temperature, and internal pressure as thermodynamically the plasma is like a gas. Laser-driven ionization also contributes to plasma density, temperature, and internal pressure. Electron density affects the plasma's electromagnetic properties and thus magnetic pressure. Plasma deformation alters the magnetic pressure as the external magnetic field is spatially non-uniform. Also, the liquid exerts hydrostatic pressure on the plasma. Physics-based models of M-LIPMM [6] are limited to the motion of one electron in a spatially uniform magnetic field. They cannot handle plasma consisting of millions of electrons in unknown initial states under the spatially non-uniform 3D fields in E-MLIP.

Our approach couples electromagnetic and mechanical models (Figs. 3a-b) to understand the impact of magnet configuration on

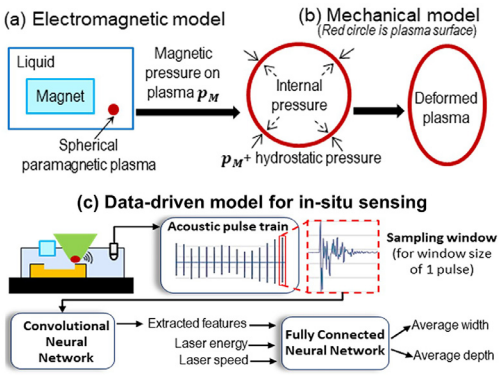

Fig. 3. Schematic of models developed in this work.

plasma shape (and thus feature dimensions). The electromagnetic model treats the plasma as a spherical body (Fig. 3a) as observed in past work for a Gaussian laser beam [1]. The plasma is assigned the permeability and permittivity of iron to capture its paramagnetic behavior [16]. The resulting magnetic pressure tensor on the plasma's surface ($\boldsymbol{p_M}$) is

$$\nabla \cdot \boldsymbol{p_M} = \boldsymbol{f} + \varepsilon\mu\partial\boldsymbol{S}/\partial t \quad (1)$$

where, $\boldsymbol{f}$ is volumetric force based on the Lorentz law, ε is dielectric permittivity, μ is magnetic permeability, $\boldsymbol{S}$ is the Poynting vector, and t is time. The number, location, and magnetization direction of the magnets was the same as in experiments. The magnet and water domains were smaller than experiments for computational feasibility, with the domain sizes increased till convergence of the computed magnetic field and pressure to eliminate spurious results. The plasma diameter was the same as that of the laser's focal spot, based on the avalanche and cascade ionization mechanisms of breakdown for nanosecond laser pulses [17].

The mechanical model predicts plasma deformation due to magnetic pressure. The plasma is treated as an elastic membrane subject to the computed magnetic pressure $\boldsymbol{p_M}$, constant isotropic hydrostatic pressure p_H from the liquid (based on Bernoulli's law), and constant internal pressure p_I. The p_I is computed based on the ideal gas assumption as

$$p_I = \rho k_B T_e \quad (2)$$

where, electron density ρ is assumed constant at the breakdown initiation value and is obtained from Vogel's equation [17], k_B is Boltzmann constant, and electron temperature T_e (assumed constant) is based on the calorimetric equation [18] and complete absorption of laser energy by the plasma. These assumptions are motivated by our focus on steady-state plasma shape as the limiting factor on feature dimensions and are based on the observation of high plasma opacity at breakdown initiation [19]. The membrane stiffness was orders of magnitude greater than the pressure components as the membrane is a modelling artifact that shouldn't affect plasma deformation. This model decouples plasma shape, electron density, and plasma permeability as it focuses on steady-state plasma shape. Nevertheless, it satisfies our goal of filling gaps in understanding the effect of E-MLIP configuration on plasma shape by introducing a key modeling capability, i.e., plasma-scale deformation under non-uniform 3D magnetic fields.

2.3. In-situ sensing and data-driven modelling

Unexpected phenomenological disturbances during machining such as plasma instability, inconsistent debris removal, and bubbles can affect the machined feature's dimensions. Quantitative prediction of feature dimensions in light of such disturbances, without offline measurement or stoppage of machining, is key for scalable control of E-MLIP. Direct measurement of disturbances is difficult due to the small length and time scales involved. Physics-based models cannot predict material removal [19,20] and regression over process

parameters ignores unexpected disturbances [21]. In-situ sensing in LIPMM can't quantify feature dimensions [22]. In-situ sensing in DLA is limited by non-quantitative classification [23], the need to stop machining [24], and neglect of channel-to-channel variation in disturbances [25]. Our approach uses acoustic waves (Fig. 1b) emitted by the E-MLIP plasma for quantitative in-situ prediction of feature dimensions [26]. The disturbances will affect the acoustic waves, e.g., via interaction with inconsistent debris ejection. The novelty lies in combining information from acoustic signals with nominal values of the process parameters to consider channel-to-channel variation in disturbances during prediction of feature dimensions. This approach contrasts with the use of only sensor signals as inputs in the laser micromachining literature. [22–26]

Fig. 3c shows our approach. The acoustic pulse train for a channel (≈ 100 s of pulses) is segmented into sampling windows with one or more pulses. Features extracted from these windows by a deep Convolutional Neural Network (CNN) are fed to a deep Fully Connected Neural Network (FCNN) along with the process parameters (laser speed and pulse energy). The FCNN outputs the channel dimensions averaged along the channel length. Separate models were created for each laser frequency. The acoustic signals were split into windows and each window and process parameter set was matched to the channel depth and width to create training and testing datasets for all the process parameter combinations. The loss function was Mean Square Error (MSE). The layer width and depth of the FCNN, number of layers of the CNN, and size of sampling window were tuned to minimize the training MSE and to ensure that the testing MSE was equal to or lesser than the training MSE (i.e., avoid overfitting).

3. Results

3.1. Impact of magnet-plasma configuration

Fig. 4a shows examples of elliptical holes machined by E-MLIP. Figs. 4b-c compare the length (major axis), width (minor axis) and depth of E-MLIP holes to the diameter and depth of the circular LIPMM holes. E-MLIP with configuration 5 yields the greatest concurrent reduction in width and enhancement relative to LIPMM while also increasing the hole length. This configuration was used to machine microchannels with laser motion perpendicular to the magnet's face so that the channel's length aligned with the hole's length. This is based on the following rationale. A channel consists of overlapping holes, wherein each hole is machined by a laser pulse. Aligning the channel length to the length of E-MLIP holes will reduce channel width relative to LIPMM since the magnetic field reduces each hole's width. Further, channel depth will increase since the magnetic field increases each hole's depth.

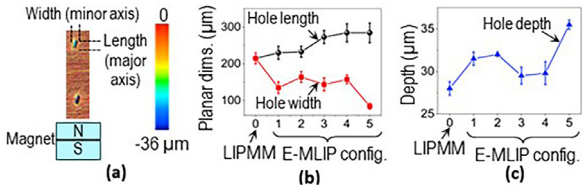

Fig. 4. (a) Elliptical E-MLIP holes with magnet-plasma configuration 5 (b-c) Change in hole dimensions with E-MLIP compared to LIPMM.

3.2. Enhanced geometric window and material removal rate

Fig. 5 compares the morphology of channels machined by E-MLIP and LIPMM. For LIPMM at 5 Hz laser frequency (Fig. 5a) an intermittent lack of machining is observed at speeds of 0.20 mm/s and above, even for the highest laser energy. Thus, the maximum laser speed for LIPMM at 5 Hz laser frequency is 0.15 mm/s. Similarly, the maximum speed is 0.25 mm/s for 10 Hz and 20 Hz frequencies respectively (Figs. 5b-c).

Figs. 5d-f show that E-MLIP does not cause intermittent lack of machining even at the highest speed of 0.65 mm/s. Thus, the highest

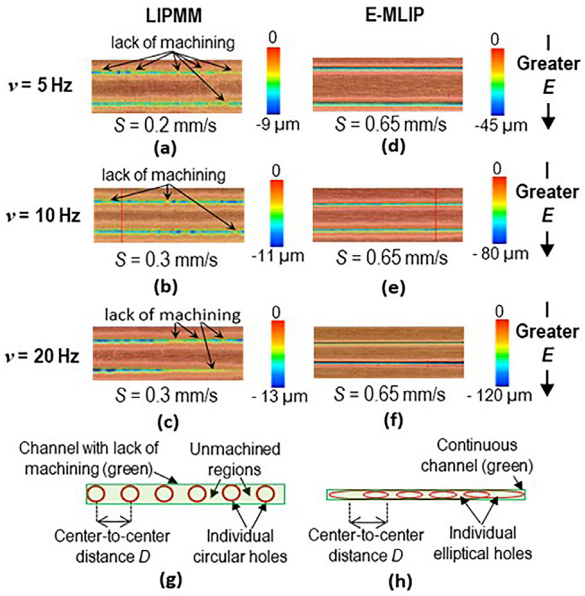

Fig. 5. Depth map of channels machined by (a-c) LIPMM (d-f) E-MLIP, where ν: laser frequency, S: laser speed, E: laser energy. Schematic of (g) Lack of machining in LIPMM (h) Consistent machining in E-MLIP.

feasible laser speed for E-MLIP is 2.5–4 times greater than that for LIPMM. M-LIPMM cannot achieve this enhancement [5–9]. For the same laser speed, energy, and frequency the center-to-center distance between adjacent holes that constitute a channel is the same for E-MLIP and LIPMM. The length of elliptical E-MLIP holes is larger than the diameter of circular LIPMM holes (Fig. 4) and is oriented along the channel's length. This increases the overlap between adjacent E-MLIP holes and ensures consistent machining (Fig. 5h-g). By corollary, for a given laser energy and frequency E-MLIP allows greater center-to-center distance, and thus greater laser speed without intermittent lack of machining.

Figs. 6a-c show the change in channel depth and width for E-MLIP relative to LIPMM (and thus to DLA). For the same process parameters and hardware E-MLIP simultaneously increases depth by 10s-100 s

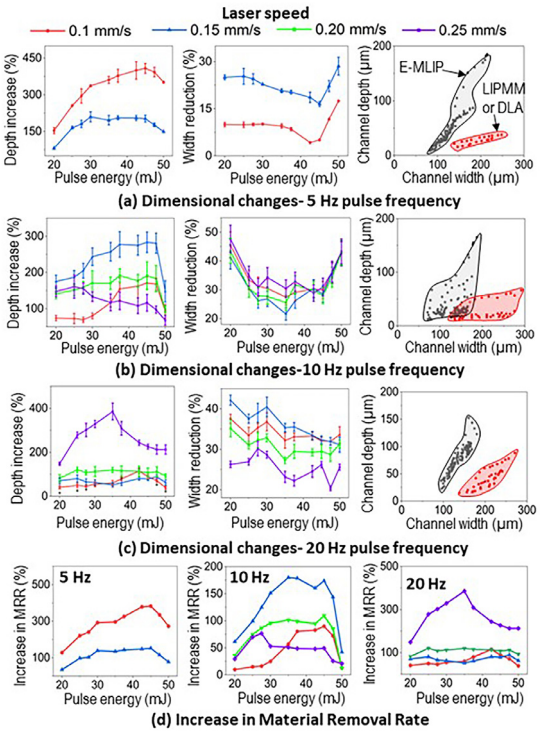

Fig. 6. E-MLIP driven change in (a-c) feature dimensions and depth-versus-width geometric window and (d) MRR, relative to LIPMM and DLA.

of % and reduces width by 10 s of %. M-LIPMM [5–9] and existing DLA variants [10–13] lack this capability. Further, Fig. 6d shows that E-MLIP increases the MRR by 15–400 % without compromising the above enhancement of feature resolution and depth. Figs. 6a-c also compare the depth-versus-width geometric window of E-MLIP to LIPMM (and thus to DLA). It is clear that E-MLIP reduces the minimum possible feature width by 30–50 % and increases the maximum possible feature depth by 200–500 %. Overall, E-MLIP simultaneously and significantly enhances feature resolution, depth and MRR relative to LIPMM and DLA beyond the reach of the state-of-the-art.

3.3. Mechanism of geometric window enhancement

Fig. 7 shows the predictions from the physics-based model. Comparing the deformed and undeformed plasma shape along the channel depth and width directions (*D* and *W*), in Fig. 7a, yields the following observations. First, for E-MLIP the concurrent increase in plasma depth and reduction in plasma width is greatest for configuration 5, which reflects the experimental effect of magnet configuration on hole dimensions in Figs. 4b-c. Our model is further qualitatively validated by noting that the predicted dependence of change in plasma dimensions on magnet configuration (Fig. 7b) is similar to experimentally observed dependence of feature depth and width in Figs. 4b-c. While the assumptions in Section 2.2 limit our model's quantitative accuracy it still captures the impact of magnet configuration in E-MLIP, which is the focus of this work.

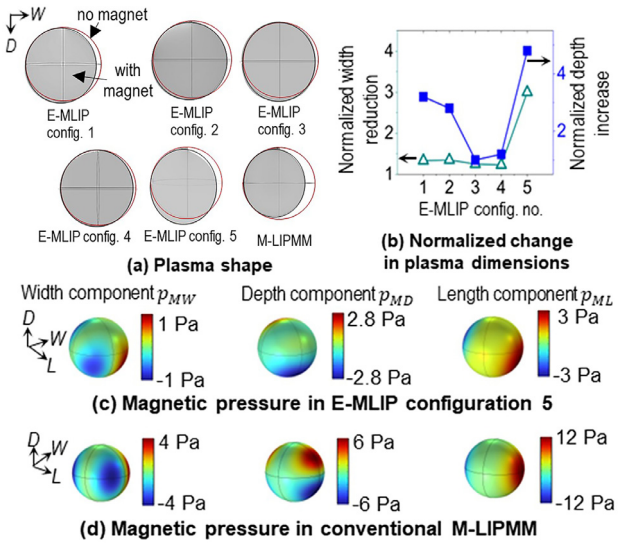

Fig. 7. Physics-based predictions of (a-b) Plasma shape and dimensions (c-d) Magnetic pressure. *D, W, L* are depth, width and length directions.

Fig. 7a also shows that unlike E-MLIP there is no change in the plasma depth for M-LIPMM, though plasma width reduces, as seen in the literature. [5–9] The reason is revealed by Figs. 7c-d which show the magnetic pressure on the plasma resolved along channel width (p_{MW}), depth (p_{MD}) and length (p_{ML}). Each magnetic field component tries to expand the plasma. Because plasma is only partly compressible its extension in one direction causes its compression in the other directions. Since hydrostatic and internal pressure are isotropic the plasma shape is driven by the competing effects of magnetic pressure components. In E-MLIP (Fig. 7c) p_{ML} and p_{MD} have similar magnitudes. Thus, the impact of p_{ML} on reducing plasma depth is strongly countered by the tendency of p_{MD} to increase plasma depth. The p_{MW} is much smaller and thus cannot counteract the tendency of p_{ML} and p_{MD} to reduce plasma width. The result is width reduction and depth increase of the plasma, and thus of the machined features, in E-MLIP. In M-LIPMM (Fig. 7d) p_{ML} is higher than p_{MW} and p_{MD}. Thus, reduction in plasma width and depth due to p_{ML}-driven expansion in plasma length overwhelms the effects of p_{MW} and p_{MD} . The result is a reduction in plasma (and feature) width without increase in depth in M-LIPMM.

3.4. In-situ prediction capability

Fig. 8 compares the measured and predicted (from data-driven model) dimensions for channels (i.e., instances) that were machined with the same process parameters but had different dimensions due to disturbances. Our predictions can differentiate between instances. This implies the ability to capture the impact of disturbances for individual features. This capability is lacking in physics-based or data-driven models that use on the process parameters as inputs. This model needs only one 5-pulse sampling window and less than one second of inference time. The in-situ and quantitative nature of the prediction will allow in-process control in the future. Note that the testing MSE with only acoustic signals as inputs, as in the literature, was 10 times higher than with our method. This demonstrates the value of our approach of combining acoustic signals and nominal process parameter values as inputs.

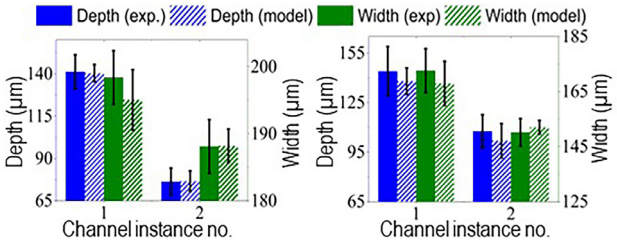

Fig. 8. Predictions from in-situ sensing. Separate instances are channels machined with same process parameters. Variance is along channel length.

4. Conclusions

The developed E-MLIP process possesses the unique ability to simultaneously increase feature resolution (by 10 s of %), feature depth (by 10s-100 s of %) and MRR (by 10s-100 s of %) relative to LIPMM and DLA. The mechanistic model reveals that anisotropic magnetic pressure drives this advance. The acoustics-based model enables novel in-situ prediction of feature dimensions in light of unknown disturbances. Our initial work has also observed that E-MLIP in a direction parallel to the magnet's face increases feature width and reduces feature depth. Our future work will pursue path-dependent magnet rotation to account for this observation during E-MLIP of non-straight-line features and will explore the impact of the magnetic field magnitude in E-MLIP.

Declaration of competing interest

The authors declare that they have no known competing financial interests or personal relationships that could have appeared to influence the work reported in this paper.

CRediT authorship contribution statement

Rajiv Malhotra: Writing – review & editing, Writing – original draft, Supervision, Resources, Project administration, Funding acquisition, Conceptualization. **AnandKumar Patel:** Writing – review & editing, Writing – original draft, Visualization, Software, Methodology, Investigation, Data curation. **Kiarash Naghavi Khanghah:** Visualization, Validation, Data curation. **Hongyi Xu:** Writing – review & editing, Resources, Funding acquisition, Data curation.

Acknowledgment

The authors acknowledge financial support by National Science Foundation grants #2336448 and #2503364 and assistance by Dr. Weihong Guo in measurements.

References

[1] Malhotra R, Saxena I, Ehmann K, Cao J (2013) Laser-induced plasma micromachining (LIPMM) for enhanced productivity and flexibility in laser-based micro-machining processes. *CIRP Annals* 62(1):211–214.

[2] Saxena I, Malhotra R, Ehmann K, Cao J (2015) High-speed fabrication of microchannels using line-based laser induced plasma micromachining. *Journal of Micro and Nano-Manufacturing* 3(2).

[3] Saxena I, Ehmann KF (2014) Multimaterial capability of laser induced plasma micromachining. *Journal of Micro and Nano-Manufacturing* 2(3):7.

[4] Pallav K, Saxena I, Ehmann KF (2014) Comparative assessment of the laser-induced plasma micromachining and the ultrashort pulsed laser ablation processes. *Journal of Micro and Nano-Manufacturing* 2(3):9.

[5] Zhang Y, Liu Y, Bhandari S, Zhang G, Deng J, Zhang Z, Ehmann K (2020) Investigation of the capabilities of transverse magnetic field controlled laser-induced plasma micro-machining. *Journal of Manufacturing Science and Engineering* 143(6).

[6] Tang H, Qiu P, Cao R, Zhuang J, Xu S (2019) Repulsive magnetic field–assisted laser-induced plasma micromachining for high-quality microfabrication. *The International Journal of Advanced Manufacturing Technology* 102(5):2223–2229.

[7] Zhang Y, Zhang Z, Zhang Y, Liu D, Wu J, Huang Y, Zhang G (2021) Study on machining characteristics of magnetically controlled laser induced plasma micromachining single-crystal silicon. *J Adv Res* 30:39–51.

[8] Chen S, Zhu W, Zhou J, Yu Y, Xie Y, Deng Y (2022) High-precision and low-damage microchannel construction via magnetically assisted laser-induced plasma ablation for micro-thermoelectric devices. *ACS Appl Mater Interfaces* 14(41):46756–46764.

[9] Zhang Y, Bhandari S, Xie J, Zhang G, Zhang Z, Ehmann K (2021) Investigation on the evolution and distribution of plasma in magnetic field assisted laser-induced plasma micro-machining. *J Manuf Process* 71:197–211.

[10] Liu Z, Wu B, Xu R, Zhao K, Shin YC (2018) Microhole drilling by double laser pulses with different pulse energies. *Journal of Manufacturing Science and Engineering* 140(9):8.

[11] Uenohara T, Takaya Y, Mizutani Y (2017) Laser micro machining beyond the diffraction limit using a photonic nanojet. *CIRP Annals* 66(1):491–494.

[12] Ye C, Cheng GJ, Tao S, Wu B (2013) Magnetic field effects on laser drilling. *Journal of Manufacturing Science and Engineering* 135(6).

[13] Muhammad N, Li L (2012) Underwater femtosecond laser micromachining of thin nitinol tubes for medical coronary stent manufacture. *Applied Physics A* 107(4):849–861.

[14] Liao K, Wang W, Mei X, Liu B (2022) High quality full ablation cutting and stealth dicing of silica glass using picosecond laser Bessel beam with burst mode. *Ceram Int* 48(7):9805–9816.

[15] Pallav K, Saxena I, Ehmann KF (2015) Laser-induced plasma micromachining process: principles and performance. *Journal of Micro and Nano-Manufacturing* 3(3):8.

[16] Hussain A, Li Q, Hao Z, Gao X, Lin J (2015) The effect of an external magnetic field on the plume expansion dynamics of laser-induced aluminum plasma*. *Plasma Science and Technology* 17(8):693.

[17] Noack J, Vogel A (1999) Laser-induced plasma formation in water at nanosecond to femtosecond time scales: calculation of thresholds, absorption coefficients, and energy density. *IEEE J Quantum Electron* 35(8):1156–1167.

[18] Rethfeld B, Kaiser A, Vicanek M, Simon G (2002) Ultrafast dynamics of nonequilibrium electrons in metals under femtosecond laser irradiation. *Physical Review B* 65(21):214303.

[19] Saxena I, Ehmann K, Cao J (2014) Laser-induced plasma in aqueous media: numerical simulation and experimental validation of spatial and temporal profiles. *Appl Opt* 53(35):8283–8294.

[20] Zhang Z, Zhang Y, Liu D, Zhang Y, Zhao J, Zhang G (2022) Bubble behavior and its effect on surface integrity in laser-induced plasma micro-machining silicon wafer. *Journal of Manufacturing Science and Engineering* 144(9).

[21] Oddiraju M, Cleeman J, Malhotra R, Chowdhury S (2025) A differentiable physics-informed machine learning approach to model laser-based micro-manufacturing process. *Journal of Manufacturing Science and Engineering* 147(5).

[22] Chen M, Malhotra R, Guo W (2023) Transfer learning for predictive quality in laser-induced plasma micro-Machining1. *Journal of Micro and Nano-Manufacturing* 10(4):9.

[23] Yildirim K, Nagarajan B, Tjahjowidodo T, Castagne S (2024) Development of a multi-sensor system for in-situ process monitoring of femtosecond laser micromachining. *The International Journal of Advanced Manufacturing Technology* 135(1):799–813.

[24] Chen X, Xu Y, Chen N-K, Shy S, Chui H-C (2021) In-situ depth measurement of laser micromachining. *Photonics* 8. https://doi.org/10.3390/photonics8110493.

[25] Kim GY, Song D-S, Kwon K-K, Ahn S-H (2024) Sound-based depth estimation of glass microchannel in laser-induced backside wet etching using wavelet transform. *International Journal of Precision Engineering and Manufacturing-Green Technology* 11(4):1081–1096.

[26] Jang H, Song H, Koh HS, Yoon T, Kwon YJ (2023) Shock wave generation in water by nanosecond pulse laser irradiation with 1064 and 2940 nm wavelengths. *Optics & Laser Technology* 167:109670.